



# Virtual element method for the numerical simulation of long-term dynamics of transitional environments

Annamaria Mazzia\*, Massimiliano Ferronato, Pietro Teatini, Claudia Zoccarato

Department of Civil, Environmental and Architectural Engineering, University of Padova, via F. Marzolo 9, 35131 Padova, Italy



## ARTICLE INFO

### Article history:

Received 6 May 2019

Received in revised form 16 December 2019

Accepted 1 January 2020

Available online 8 January 2020

### Keywords:

Virtual element method

Numerical modeling

Transitional environments

Long-term dynamics

Large deformation

## ABSTRACT

The prediction of long-term dynamics of transitional environments, e.g., lagoon evolution, salt-marsh growth or river delta progradation, is an important issue to estimate the potential impacts of different scenarios on such vulnerable intertidal morphologies. The numerical simulation of the combined accretion and consolidation, i.e., the two main processes driving the dynamics of these environments, however, suffers from a significant geometric non-linearity, which may result in a pronounced grid distortion using standard grid-based discretization methods. The present work describes a novel numerical approach, based on the Virtual Element Method (VEM), for the long-term simulation of the vertical dynamics of transitional landforms. The VEM is a grid-based variational technique for the numerical discretization of Partial Differential Equations (PDEs) allowing for the use of very irregular meshes consisting of a free combination of different polyhedral elements. The model solves the groundwater flow equation, coupled to a geomechanical module based on Terzaghi's principle, in a large-deformation setting, taking into account both the geometric and the material non-linearity. The use of the VEM allows for a great flexibility in the element generation and management, avoiding the numerical issues connected with the adoption of strongly distorted meshes. The numerical model is developed, implemented and tested in real-world examples, showing an interesting potential for addressing complex environmental situations.

© 2020 Elsevier Inc. All rights reserved.

## 1. Introduction

Lagoons, deltas and estuaries are coastal environments characterized by a significant ecological and socio-economic value. Since the geomorphological equilibrium of these landforms is regulated by complex interactions involving the variation of the sea level and land elevation, the possible primary production and sediment deposition rate [1], the analysis of their stratigraphies often plays a key role for the reconstruction of the sea-level evolution and the distribution of the Holocene sediments [2–4]. For these reasons, a number of research projects on transitional environments are under way worldwide, e.g. [5–7], with the aim at achieving a more reliable interpretation of the sea-level evolution under future scenarios.

The rise and/or lowering of the surface elevation of these vulnerable structures is controlled by a number of interacting factors. Typically, the active sediment deposition and compaction rate are the most important driving mechanisms, along with the possible presence of external forcing actors such as the sea level rise (SLR), deep subsidence, sediment availability,

\* Corresponding author.

E-mail addresses: [annamaria.mazzia@unipd.it](mailto:annamaria.mazzia@unipd.it) (A. Mazzia), [massimiliano.ferronato@unipd.it](mailto:massimiliano.ferronato@unipd.it) (M. Ferronato), [pietro.teatini@unipd.it](mailto:pietro.teatini@unipd.it) (P. Teatini), [claudia.zoccarato@unipd.it](mailto:claudia.zoccarato@unipd.it) (C. Zoccarato).

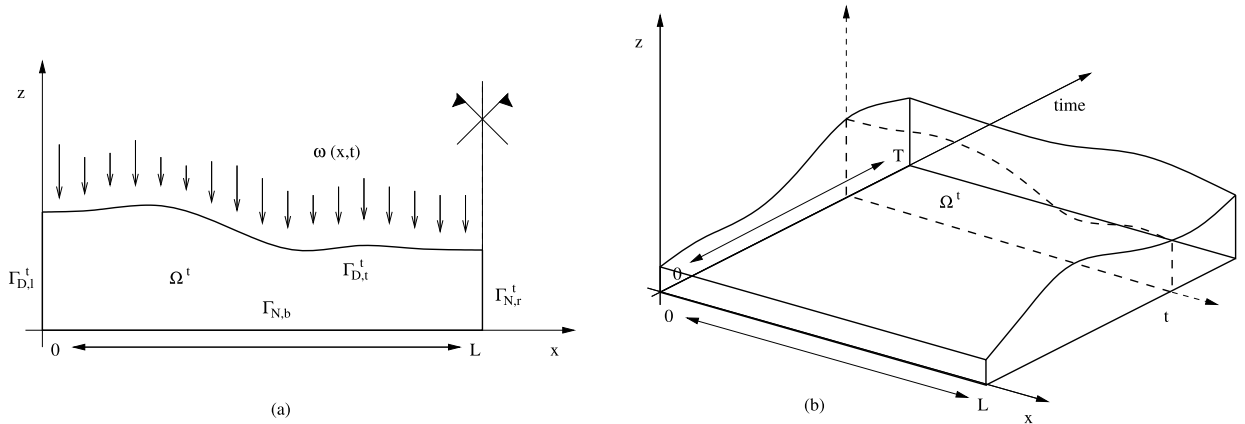


Fig. 1. Sketch of the problem domain at some instant  $t$  (a) and for the full simulation (b).

tidal and wave regimes, and erosion [1,8]. Despite its importance, the compaction term is often computed with simplified approaches, such as empirical relationships [9,10] and 1D or point models [11–13]. A coupled geomechanical approach in a 2D framework has been advanced only recently by Zoccarato and Teatini [14], where the groundwater flow equation is combined with a vertical compaction model in a large deformation setting. A major difficulty in the model formulation, however, stems from the significant geometric and material non-linearities that characterize the freshly deposited sediments, which require the definition of a spatial domain that changes in time as the system progressively evolves. From a numerical point of view, this means that the computational grid must be modified at every discrete time value, with the starting cells undergoing very pronounced distortions in simulations reproducing long-term evolutions, i.e., spanning hundreds or even thousands of years.

Solutions by standard Finite Element approaches may suffer from the difficulty of adapting to the pronounced domain distortion. Remeshing strategies can be applied, but are usually computationally expensive efforts, especially on consideration of the domain modification in time. To avoid the drawbacks associated to the requirement of a topologically consistent grid, several methods have been developed in recent years. For instance, we mention meshless and hybrid techniques, e.g., [15–21], which have been also employed in the context of geological problems [22,23]. Another alternative for handling generally irregular polyhedral grids is the Virtual Element Method (VEM). The VEM approach is a grid-based variational technique for the numerical discretization of Partial Differential Equations (PDEs) allowing for the use of very irregular meshes consisting of a free combination of different polyhedral elements. The VEM was first introduced in the context of mimetic finite differences [24] and then recast in the framework of classical variational formulations [25,26]. Mainly because of its flexibility, this discretization strategy has attracted a growing interest, with emerging applications in elasticity, geomechanics and flow in fracture networks, e.g., [27–33].

The present work describes the simulation of the long-term dynamics of a transitional environment with the aid of the VEM. The governing equations are based on the physically-based approach developed in [14], where the pore pressure evolution within a compacting/accreting vertical cross-section of the landform is coupled to a geomechanical module computing the vertical (large) deformation of the porous medium. Soil properties, such as porosity, permeability, and compressibility, vary with the effective intergranular stress according to empirical non-linear constitutive relationships. The geometric non-linearity is accounted for by a Lagrangian approach with an adaptive polyhedral grid, where new elements are added to follow the sedimentation and distorted elements are automatically joined to adjacent cells according to the deposit consolidation. In particular, the last feature can take great advantage from the VEM flexibility in the element generation and management, avoiding the numerical difficulties arising from strongly distorted grids.

The paper is organized as follows. First, the governing equations of the model are recalled. Then, the VEM concepts are introduced and applied to obtain the numerical formulation. Computational results are presented to validate the proposed approach and show its potential in the management of distorted grids. Finally, a real-world example simulating the long-term evolution of the Mekong river delta, Vietnam, is discussed, with a few conclusive remarks closing the presentation.

## 2. Governing PDEs for the prediction of the long-term dynamics of transitional environments

We follow the modeling approach developed in [14]. Let  $\Omega^t \subset \mathbb{R}^2$  denote the vertical cross-section of length  $L$  in the  $x-z$  reference system of the landform at some instant  $t \in I = ]0, T[$ , with  $T$  the final simulation time. The boundary of  $\Omega^t$ ,  $\Gamma^t$ , is subdivided into four portions (Fig. 1):

1.  $\Gamma_{N,b} = \{\mathbf{x} = (x, z) : x \in [0, L], z = 0\}$ , i.e., the bottom boundary, represents the impervious landform basement;
2.  $\Gamma_{N,r}^t = \{\mathbf{x} = (x, z) : x = L, z > 0\}$ , i.e., the right boundary, is assumed to be a symmetry axis for the landform cross-section, hence no cross-flow is allowed;

3.  $\Gamma_{D,l}^t = \{\mathbf{x} = (x, z) : x = 0, z > 0\}$ , i.e., the left boundary, represents the outer landform limit that is in equilibrium with the tidal creek, which means that no overpressure with respect to the hydrostatic distribution is allowed;
4.  $\Gamma_{D,t}^t = \Gamma^t \setminus (\Gamma_{N,b} \cup \Gamma_{N,r}^t \cup \Gamma_{D,l}^t)$ , i.e., the top boundary, is kept at hydrostatic pressure.

We denote as  $\Gamma_N^t = \Gamma_{N,b} \cup \Gamma_{N,r}^t$  and  $\Gamma_D^t = \Gamma_{D,l}^t \cup \Gamma_{D,t}^t$  the portions of boundary where Neumann and Dirichlet conditions, respectively, are prescribed at every instant  $t \in I$ , with  $\mathbf{n}$  the outer normal vector. As usual,  $\Gamma_D^t \cup \Gamma_N^t = \Gamma^t$  and  $\Gamma_D^t \cap \Gamma_N^t = \emptyset$ . A bar above a set identifies the union of the set with its boundary, i.e.,  $\overline{\Omega^t} = \Omega^t \cup \Gamma^t$ . The pore pressure variation,  $p$ , with respect to hydrostatic conditions, in  $\overline{\Omega} = \overline{\Omega^t} \times I$ , is governed by the fluid mass balance in a deforming and saturated porous medium. Following the developments originally advanced in [34,35], the mass balance equation has to take care of: (i) large solid grain motion; (ii) Darcy's law applied to the relative velocity between fluid and solid grains; (iii) incompressible solid grains. The landform accretion depends on the amount of sediment deposition rate,  $\omega(x, t)$ , which causes a variation in time of the total vertical stress,  $\hat{\sigma}_z(\mathbf{x}, t)$ , relative to the initial total vertical stress. The physical processes leading to a vertical compaction are the most significant with respect to other effects [36], hence only a motion along the  $z$ -direction is allowed. The vertical displacement,  $u(\mathbf{x}, t)$ , is obtained as a function of the variation of the vertical effective stress,  $\sigma_z(\mathbf{x}, t)$ , which is related to  $\hat{\sigma}_z(\mathbf{x}, t)$  by Terzaghi's principle [37]. Hence, the strong form of the initial/boundary value problem may be stated as follows.

Given  $\omega : [0, L] \times I \rightarrow \mathbb{R}$ , find  $p : \overline{\Omega} \rightarrow \mathbb{R}$  and  $u : \overline{\Omega} \rightarrow \mathbb{R}$  such that:

$$\psi \dot{p} - \nabla \cdot \left( \frac{\kappa}{\gamma} \nabla p \right) = \zeta \dot{\hat{\sigma}}_z \quad \text{on } \Omega^t \times I \quad \text{(fluid mass balance)} \quad (1)$$

$$\dot{\hat{\sigma}}_z = (1 - \phi_0) (\gamma_s - \gamma) \omega \quad \text{on } \Omega^t \times I \quad \text{(total stress variation)} \quad (2)$$

$$\sigma_z + p = \hat{\sigma}_z \quad \text{on } \Omega^t \times I \quad \text{(Terzaghi's principle)} \quad (3)$$

$$u + \int_0^z \frac{\alpha \sigma_z}{1 - \alpha \sigma_z} dz = 0 \quad \text{on } \Omega^t \times I \quad \text{(vertical grain motion)} \quad (4)$$

$$-\frac{\kappa}{\gamma} \nabla p \cdot \mathbf{n} = 0 \quad \text{on } \Gamma_N^t \times I \quad \text{(no-flow boundary conditions)} \quad (5)$$

$$p = 0 \quad \text{on } \Gamma_D^t \times I \quad \text{(homogeneous essential conditions)} \quad (6)$$

$$p(\mathbf{x}, 0) = 0 \quad \forall \mathbf{x} \in \overline{\Omega^0} \quad \text{(initial conditions)} \quad (7)$$

where  $\psi$  is the storage coefficient,  $\kappa$  is the rank-2 hydraulic conductivity tensor,  $\gamma$  the specific weight of water,  $\zeta$  the soil oedometric compressibility;  $\phi_0$  is the porosity at the initial reference vertical stress  $\sigma_{z,0}$ ,  $\gamma_s$  the specific weight of the solid grains;  $\alpha$  is the classical compressibility as a function of the soil Young's modulus and Poisson's ratio,  $E$  and  $\nu$ , respectively;  $\nabla \cdot$  and  $\nabla$  are the divergence and gradient operator, respectively; the superposed dot,  $\dot{(\cdot)}$ , denotes a derivative with respect to time. With respect to the formulation developed in [37], the use of a Lagrangian approach allows us to replace in (1) the total Eulerian derivatives on a moving particle with partial derivatives in time.

The governing PDE (1) is strongly non-linear when equipped with appropriate constitutive laws for the material under consideration. Having defined the classical compressibility  $\alpha$  as  $(1 - 2\nu)(1 + \nu)/[(1 - \nu)E]$ , the following relationships hold for  $\psi$  and  $\zeta$  [14,37]:

$$\psi = \zeta + \phi\beta \quad \text{(storage coefficient)} \quad (8)$$

$$\zeta = \frac{\sigma_z \frac{d\alpha}{d\sigma_z} + \alpha}{1 - \alpha \sigma_z} \quad \text{(oedometric compressibility)} \quad (9)$$

with  $\beta$  the groundwater compressibility and  $\phi$  the soil porosity. Moreover,  $\kappa$ ,  $\phi$ , and  $\alpha$  vary with  $\sigma_z$  according to empirical relationships which depend on the sediment type [14].

### 3. The Virtual Element Method

The numerical solution to the initial boundary value problem (1)-(7) is obtained by the VEM. In particular, we apply the method of order 1 with respect to the literature. The classical Galerkin weak form of equation (1) with the homogeneous boundary conditions (5)-(6) reads as follows.

Find  $p(t) \in \mathcal{V}(\Omega^t)$  such that  $\forall t \in [0, T]$ :

$$\int_{\Omega^t} \frac{\kappa}{\gamma} \nabla v \cdot \nabla p \, d\Omega^t + \int_{\Omega^t} \psi v \dot{p} \, d\Omega^t = \int_{\Omega^t} \zeta v \dot{\hat{\sigma}}_z \, d\Omega^t, \quad \forall v \in \mathcal{V}(\Omega^t) \quad (10)$$

where  $\mathcal{V}(\Omega^t) = \{v \in H^1(\Omega^t), v = 0 \text{ on } \Gamma_D^t\}$  and, as usual,  $H^1$  is the Sobolev space of square integrable functions with square integrable gradients.

In a more compact way, equation (10) can be written as:

$$a(v, p) + b(v, p) = l(v), \quad \forall v \in \mathcal{V}(\Omega^t) \tag{11}$$

by defining the bilinear forms

$$a(v, p) = \int_{\Omega^t} \frac{\kappa}{\gamma} \nabla v \cdot \nabla p \, d\Omega^t, \quad b(v, p) = \int_{\Omega^t} \psi v \dot{p} \, d\Omega^t, \tag{12}$$

and the linear functional

$$l(v) = \int_{\Omega^t} \zeta v \dot{\alpha}_z \, d\Omega^t. \tag{13}$$

The bilinear forms  $a(\cdot, \cdot)$  and  $b(\cdot, \cdot)$  are continuous and coercive and the linear functional  $l(\cdot)$  is continuous, since:

1.  $\Omega^t$  is a bounded, open, polygonal subset of  $\mathbb{R}^2$ ;
2. the tensor  $\kappa/\gamma$  is bounded, measurable, symmetric and strongly elliptic, that is, there exist two positive constants,  $k_*$  and  $k^*$ , such that for every  $\mathbf{v} \in \Omega^t$  the following inequality holds:

$$k_* \|\mathbf{v}\|^2 \leq \mathbf{v} \cdot \frac{\kappa}{\gamma} \mathbf{v} \leq k^* \|\mathbf{v}\|^2, \tag{14}$$

where  $\|\mathbf{v}\|$  is the usual Euclidean norm of the vector  $\mathbf{v}$ ;

3. the storage coefficient  $\psi$  and the oedometric compressibility  $\zeta$  are functions in  $L^2(\Omega^t)$ .

Thus, problem (11) is well-posed and existence and uniqueness of the weak solution follow from the Lax-Milgram theorem [38].

Let  $\mathcal{T}_h^t$  be a finite partition of  $\Omega^t$  into non-overlapping and non-empty polygonal elements  $E$ , not necessarily convex. Two consecutive edges are also allowed to form a flat angle, that is hanging nodes are geometrically possible in the mesh. As usual,  $h$  denotes the maximum of the diameters of the elements in  $\mathcal{T}_h^t$ . For each polygon  $E$ , we denote by  $\mathbf{x}_i^E = (x_i^E, z_i^E)$  and  $e_i, i = 1, \dots, N^E$ , the vertices, listed in an anti-clockwise order, and the edge connecting  $\mathbf{x}_i^E$  and  $\mathbf{x}_{i+1}^E$ , or  $\mathbf{x}_1^E$  if  $i = N^E$ , respectively. Then, we can define:

- the element diameter  $h_E$ :

$$h_E = \max_{i=1, \dots, N^E} \sqrt{(x_{i+1}^E - x_i^E)^2 + (z_{i+1}^E - z_i^E)^2}, \tag{15}$$

hence  $h = \max_{E \in \mathcal{T}_h^t} (h_E)$ ;

- the element area  $|E|$ :

$$|E| = \frac{1}{2} \left| \sum_{i=1}^{N^E} (x_i^E z_{i+1}^E - x_{i+1}^E z_i^E) \right|; \tag{16}$$

- the element centroid  $\mathbf{x}_E = (x_E, z_E)$

$$x_E = \frac{\sum_{i=1}^{N^E} x_i^E}{N^E}, \quad z_E = \frac{\sum_{i=1}^{N^E} z_i^E}{N^E}. \tag{17}$$

Let  $n$  and  $n_{el}$  be the total number of nodes and elements of the partition  $\mathcal{T}_h^t$ . We denote by  $\mathcal{P}_1(E)$  the space of polynomials of degree at most 1 in  $E$ , with  $\dim(\mathcal{P}_1) = 3$  and  $\mathcal{P}_1(E) = \text{span}\{m_1, m_2, m_3\}$ , being:

$$m_1(x, z) = 1, \quad m_2(x, z) = \frac{x - x_E}{h_E}, \quad m_3(x, z) = \frac{z - z_E}{h_E} \tag{18}$$

the scaled monomial functions. Now, we can define as  $a^E(v, p)$ ,  $b^E(v, p)$ , and  $l^E(v)$  the bilinear forms in (12) and the linear functional in (13), respectively, restricted to the cell  $E$ , such that:

$$a(v, p) = \sum_{E \in \mathcal{T}_h^t} a^E(v, p), \quad b(v, p) = \sum_{E \in \mathcal{T}_h^t} b^E(v, p), \quad l(v) = \sum_{E \in \mathcal{T}_h^t} l^E(v), \quad \forall v, p \in \mathcal{V}. \tag{19}$$

The global finite dimensional space  $\mathcal{V}_h \subset \mathcal{V}$ , associated to the partition  $\mathcal{T}_h^t$ , is defined such that the restriction of every virtual element function  $v_h$  to the mesh element  $E$  belongs to  $\mathcal{V}_{h|E}$ :

$$\mathcal{V}_h = \{v_h \in H^1(\Omega^t) : v_{h|E} \in \mathcal{V}_{h|E} \text{ for every } E \in \mathcal{T}_h^t\}. \tag{20}$$

We require that  $\mathcal{P}_1(E) \subset \mathcal{V}_{h|E}$  and the bilinear forms  $a^E(v, p)$  and  $b^E(v, p)$  can be computed exactly for any  $v \in \mathcal{P}_1(E)$  and any  $p \in \mathcal{V}_{h|E}$ . The construction of this space is carried out by three steps:

- (i) we select the set of degrees of freedom that uniquely characterizes the local spaces;
- (ii) we introduce the elliptic projection operator onto polynomials, which makes the local bilinear forms computable using only the selected degrees of freedom;
- (iii) we define the virtual element functions making use of this elliptic projector.

As to point (i), we assume that each virtual element function  $v_h$  restricted to the polygonal cell  $E$  is uniquely defined by its values at the vertices of  $E$ . Then, for point (ii), we introduce the elliptic projection operator  $\Pi_1^\nabla : H^1(E) \cap C^0(\bar{E}) \rightarrow \mathcal{P}_1(E)$ , so that the elliptic projection of a function  $v_h$  is the linear polynomial that satisfies the variational problem:

$$\int_E \nabla \Pi_1^\nabla v_h \cdot \nabla q \, d\mathbf{x} = \int_E \nabla v_h \cdot \nabla q \, d\mathbf{x} \quad \forall q \in \mathcal{P}_1(E), \tag{21}$$

with the additional condition that

$$\int_{\partial E} \Pi_1^\nabla v_h \, ds = \int_{\partial E} v_h \, ds. \tag{22}$$

Finally, in point (iii) we define the conforming virtual element space of order 1 as

$$\mathcal{V}_{h|E} = \left\{ v_h \in H^1(E) : v_{h|\partial E} \in C^0(\partial E), v_{h|e} \in \mathcal{P}_1(e) \forall e \in \partial E, \nabla^2 v_h \in \mathcal{P}_1(E), \int_E (v_h - \Pi_1^\nabla v_h) q \, d\mathbf{x} = 0 \forall q \in \mathcal{P}_1(E) \right\}. \tag{23}$$

By equations (21)-(23), note that:

1. the definition of the virtual element space uses the *enhancement* strategy introduced in [39];
2. the degrees of freedom (vertex values) of each virtual element function are unisolvent in the virtual element space;
3. the polynomial space  $\mathcal{P}_1(E)$  is a subset of  $\mathcal{V}_{h|E}$ .

The explicit expression for  $\Pi_1^\nabla v_h$  is given by [26,40,41]:

$$\Pi_1^\nabla v_h = (\mathbf{x} - \mathbf{x}_E) \cdot \frac{1}{|E|} \int_E \nabla v_h \, d\mathbf{x} + \bar{v}_h, \tag{24}$$

where

$$\bar{v}_h = \frac{1}{N^E} \sum_{i=1}^{N^E} v_h(\mathbf{x}_i^E). \tag{25}$$

The right-hand side of (24) can be easily obtained by knowing  $v_h$  on  $\partial E$ . Since  $\int_E \nabla v_h \, d\mathbf{x} = \int_{\partial E} v_h \mathbf{n}_{\partial E} \, ds$ , with  $\mathbf{n}_{\partial E}$  the outer normal to  $\partial E$ , the integral is exactly computed through the trapezoidal rule, which requires only the values of  $v_h$  at the vertices of  $E$ , i.e., the selected degrees of freedom.

We introduce also the  $L^2$ -orthogonal projection  $\Pi_1^0 : H^1(E) \cap C^0(\bar{E}) \rightarrow \mathcal{P}_1(E)$  such that the variational problem:

$$\int_E \Pi_1^0(v_h) q \, d\mathbf{x} = \int_E v_h q \, d\mathbf{x}, \quad \forall q \in \mathcal{P}_1(E), \tag{26}$$

holds. By using the enhancement strategy mentioned above, the orthogonal projector  $\Pi_1^0$  coincides with the elliptic projector  $\Pi_1^\nabla$  [39]. It is worth mentioning that this property holds only for the enhanced virtual element spaces containing linear and quadratic polynomials, and no longer holds for higher order spaces.

The basis functions  $\varphi_i$  of the space  $\mathcal{V}_{h|E}$  satisfy the classical interpolation property:

$$\varphi_i(\mathbf{x}_j^E) = \delta_{ij}, \quad i, j = 1, \dots, N^E, \tag{27}$$

with  $\delta_{ij}$  the Kronecker delta, and are not known explicitly in  $E$ . In other words, the basis function of the finite approximation space  $\mathcal{V}_h$  associated to the grid node  $k$ : (i) takes value 1 on  $k$  and 0 on the other nodes, (ii) is piecewise linear along the boundary of the polygons sharing  $k$ , (iii) has a local support made by the union of the polygons sharing  $k$ , and (iv) is not known explicitly within those polygons, but is such that the divergence of its gradient is zero. It is easy to observe that the basis functions of linear finite elements satisfy these properties, hence they can be considered as a special case of virtual elements.

### 3.1. Local stiffness matrix

The stiffness matrix resulting from the discretization of problem (10) is obtained by assembling the elemental contributions arising from the computation of  $a^E(\varphi_i, \varphi_j)$ ,  $i, j = 1, \dots, N^E$ . To this aim, we exploit the fact that we are able to compute  $a^E(\Pi_1^\nabla \varphi_i, \Pi_1^\nabla \varphi_j)$  through equation (24), even though  $\varphi_i$  and  $\varphi_j$  are not known in  $E$ . Using Pythagora's identity and assuming that  $\kappa/\gamma$  is constant over the polygon  $E$ , we can decompose  $a^E(\varphi_i, \varphi_j)$  as:

$$a^E(\varphi_i, \varphi_j) = a^E(\Pi_1^\nabla \varphi_i, \Pi_1^\nabla \varphi_j) + a^E((1 - \Pi_1^\nabla)\varphi_i, (1 - \Pi_1^\nabla)\varphi_j), \quad i, j = 1, \dots, N^E. \quad (28)$$

The first contribution to the right-hand side of (28) can be computed exactly and gives rise to the so-called *consistency* matrix  $\mathbf{K}_C^{VEM}$ :

$$(\mathbf{K}_C^{VEM})_{ij} = \int_E \frac{\kappa}{\gamma} \nabla \Pi_1^\nabla \varphi_i \cdot \nabla \Pi_1^\nabla \varphi_j \, d\mathbf{x}, \quad i, j = 1, \dots, N^E, \quad (29)$$

while the second term:

$$(\mathbf{K}_S^E)_{ij} = \int_E \frac{\kappa}{\gamma} \nabla(1 - \Pi_1^\nabla)\varphi_i \cdot \nabla(1 - \Pi_1^\nabla)\varphi_j \, d\mathbf{x}, \quad i, j = 1, \dots, N^E, \quad (30)$$

cannot be usually handled and is therefore replaced by a *stability* matrix,  $\mathbf{K}_S^{VEM}$ , whose role is to guarantee the ellipticity of  $a^E$ . The final VEM stiffness matrix reads:

$$\mathbf{K}^{VEM} = \mathbf{K}_C^{VEM} + \mathbf{K}_S^{VEM} \quad (31)$$

Details on the practical computation of  $\mathbf{K}^{VEM}$  are provided in Appendix A.

### 3.2. Local mass matrix

The construction of the local mass matrix is performed similarly to the stiffness matrix. First of all, as usual, we assume that the dependence on time of the unknown function  $p(t)$  in the weak formulation (10) is lumped in the coefficients linearly combining the basis functions. Collecting the time derivatives out of the integral in space, we can focus on the following auxiliary local bilinear form  $\hat{b}^E$  associated to  $b^E$ :

$$\hat{b}^E(v, p) = \int_E \psi v p \, d\mathbf{x}, \quad v, p \in \mathcal{V}. \quad (32)$$

Following equation (26), we apply the  $L^2$ -orthogonal projection  $\Pi_1^0$ :

$$\hat{b}^E(\Pi_1^0 v, u) = \hat{b}^E(v, u), \quad (33)$$

which requires:

$$\int_E (v - \Pi_1^0 v) u \, d\mathbf{x} = 0, \quad \forall u \in \mathcal{P}_1(E), \quad (34)$$

i.e., the complement of the projection is orthogonal to any linear polynomial in  $E$ . The mass matrix resulting from the discretization of problem (10) is obtained by assembling the elemental contributions arising from  $\hat{b}^E(\varphi_i, \varphi_j)$ ,  $i, j = 1, \dots, N^E$ . Using Pythagora's identity as in (28) and assuming  $\psi$  constant over the polygon  $E$ , we have

$$\hat{b}^E(\varphi_i, \varphi_j) = \hat{b}^E(\Pi_1^0 \varphi_i, \Pi_1^0 \varphi_j) + \hat{b}^E((1 - \Pi_1^0)\varphi_i, (1 - \Pi_1^0)\varphi_j), \quad i, j = 1, \dots, N^E. \quad (35)$$

We can decompose the mass matrix into the sum of two contributions. The first contribution to the right-hand side of (35) is the *consistency* matrix  $\mathbf{M}_C^{VEM}$ :

$$(\mathbf{M}_C^{VEM})_{ij} = \int_E \psi \Pi_1^0 \varphi_i \Pi_1^0 \varphi_j \, d\mathbf{x}, \quad i, j = 1, \dots, N^E. \quad (36)$$

The second contribution:

$$(\mathbf{M}_S^*)_{ij} = \int_E \psi (1 - \Pi_1^0) \varphi_i (1 - \Pi_1^0) \varphi_j \, d\mathbf{x}, \quad i, j = 1, \dots, N^E, \quad (37)$$

cannot be computed exactly and is approximated by a stability matrix  $\mathbf{M}_S^{VEM}$ . Hence, the final VEM mass matrix reads:

$$\mathbf{M}^{VEM} = \mathbf{M}_C^{VEM} + \mathbf{M}_S^{VEM} \quad (38)$$

Details on the practical computation of  $\mathbf{M}^{VEM}$  are provided in Appendix A.

### 3.3. Forcing term and boundary conditions

The forcing term can be computed by exploiting again the properties of the projection operator  $\Pi_1^0$ . In fact:

$$\int_E \overline{(\zeta \dot{\sigma}_z)} v \, d\mathbf{x} = \int_E \overline{(\zeta \dot{\sigma}_z)} \Pi_1^0 v \, d\mathbf{x}, \quad \forall v \in \mathcal{V}_{h|E} \quad (39)$$

where  $\overline{(\zeta \dot{\sigma}_z)}$  is the average value of  $(\zeta \dot{\sigma}_z)$  as defined in (25). The left-hand side of equation (39) can be used as an approximation,  $\hat{l}^E(v)$ , of the exact linear form  $l^E(v)$ , which corresponds to the application of the midpoint rule for computing numerically the integral over the polygon  $E$ . Such an approximation does not introduce any deviation from the optimal convergence of the VEM in  $H^1(\Omega^t)$  [25,26].

The local term,  $(\mathbf{b}_E)_i$ , to be assembled in the  $i$ -th component of the discrete right-hand side of equation (10), is given by  $\hat{l}^E(\varphi_i)$ , i.e.:

$$(\mathbf{b}_E)_i = \overline{(\zeta \dot{\sigma}_z)} \int_E \Pi_1^0 \varphi_i \, d\mathbf{x}, \quad i = 1, \dots, N^E, \quad (40)$$

where  $\Pi_1^0 \varphi_i$  is computed with the aid of equation (26). Details on the practical implementation are given in Appendix A, equations (A.7)-(A.8). Application of the midpoint rule to the integral in (40) simply leads to:

$$(\mathbf{b}_E)_i = \zeta(\mathbf{x}_E) \dot{\sigma}_z(\mathbf{x}_E) \frac{|E|}{N^E}, \quad i = 1, \dots, N^E. \quad (41)$$

Finally, prescription of the homogeneous Dirichlet conditions (6) is trivially accomplished as in the standard Finite Element method because of the interpolation property (27). The basis functions associated with the boundary vertices are removed from the formulation, and, at the implementation level, the conditions of Dirichlet type are strongly imposed. Zero Neumann conditions are implicitly satisfied.

### 3.4. Non-linear solution algorithm

The VEM discretization described in the previous sections leads to the system of non-linear ordinary differential equations in time:

$$\mathbf{K}(\mathbf{p})\mathbf{p} + \mathbf{M}(\mathbf{p})\frac{d\mathbf{p}}{dt} = \mathbf{b}(\mathbf{p}, t) \quad (42)$$

where  $\mathbf{K}$ ,  $\mathbf{M}$  and  $\mathbf{b}$  are the global stiffness, mass and right-hand side, respectively, and  $\mathbf{p}$  collects the values of  $p(t)$  on the nodes of the computational grid. The non-linear system (42) is first integrated in time by a standard  $\vartheta$ -method, then solved at each discrete time-level by a fixed-point iteration:

$$\left[ \vartheta \Delta t \mathbf{K}(\mathbf{p}_\tau^k) + \mathbf{M}(\mathbf{p}_\tau^k) \right] \mathbf{p}_{t+\Delta t}^{k+1} = \left[ \mathbf{M}(\mathbf{p}_\tau^k) - (1 - \vartheta) \Delta t \mathbf{K}(\mathbf{p}_\tau^k) \right] \mathbf{p}_t + \Delta t \left[ \vartheta \mathbf{b}_{t+\Delta t}(\mathbf{p}_\tau^k) + (1 - \vartheta) \mathbf{b}_t(\mathbf{p}_\tau^k) \right] \quad (43)$$

with  $\vartheta \in [0.5, 1]$  a user-specified parameter,  $\Delta t$  the time-step size,  $k$  the non-linear iteration counter, and  $\tau = \vartheta(t + \Delta t) + (1 - \vartheta)t$  an intermediate instant between  $t$  and  $t + \Delta t$ .

Usually, the non-linear functions describing the material parameters  $\kappa(\sigma_z)$ ,  $\alpha(\sigma_z)$ ,  $\phi(\sigma_z)$ , and  $\zeta(\sigma_z)$  are derived from available lab or field experiments and do not have an explicit analytical expression. This prevents from the use of a Newton approach and makes a rigorous convergence analysis of the scheme (43) not possible in general. Computational experiences with real material data provide a relatively fast convergence of the fixed-point iteration (less than 10 iterations) if the

time-step size is sufficiently small, i.e., on the order of 1 year for simulations spanning thousands of years. This result, however, cannot be generalized.

At the beginning of each time period, the sedimentation thickness,  $\omega(\mathbf{x}, t) \cdot \Delta t$ , is computed to account for the material deposited during the current step. The first iteration of the fixed-point scheme (43) is performed, with the computation of the current nodal pressure values  $\mathbf{p}_{t+\Delta t}^{k+1}$ . The corresponding vertical stress values at the nodal level are computed with the aid of equation (3) and used to update the diffusivity tensor  $\kappa$ , porosity  $\phi$ , compressibility  $\alpha$ , and oedometric compressibility  $\zeta$ . Then, the current nodal vertical displacement  $u$  is obtained by equation (4) and the grid nodes are moved accordingly. At this point, a new iteration of the fixed-point scheme starts. Convergence is achieved when  $\|\mathbf{p}_{t+\Delta t}^{k+1} - \mathbf{p}_{t+\Delta t}^k\|_\infty$  is smaller than some prescribed exit tolerance  $\varepsilon$ . The current time value is updated, with polygons introduced on top to discretize the actual  $\Omega^f$  and the total stress  $\hat{\sigma}_z$  updated through equation (2), until the final time  $T$  is achieved or overcome. A sketch of the overall solution procedure is provided in Algorithm 1.

---

**Algorithm 1** ALGORITHM OF THE NON-LINEAR SCHEME.
 

---

1. Set  $t = 0$  and  $\mathbf{p}_t = \mathbf{0}$
  2. Compute  $\hat{\sigma}_z$  and  $\sigma_z$
  3. Update  $\kappa(\sigma_z)$ ,  $\phi(\sigma_z)$ ,  $\alpha(\sigma_z)$ ,  $\zeta(\sigma_z)$
  4. **while**  $t < T$
  5.   Set  $k = 0$
  6.   Set  $\tau = \vartheta(t + \Delta t) + (1 - \vartheta)t$  and  $\mathbf{p}_{t+\Delta t}^k = \mathbf{p}_t$
  7.   Compute  $\omega(\mathbf{x}, t) \cdot \Delta t$  for all nodes lying on  $\Gamma_{D,t}^f$
  8.   Update  $\hat{\sigma}_z = (1 - \phi_0)(\gamma_s - \gamma)\omega\Delta t$
  9.   **while**  $\|\mathbf{p}_{t+\Delta t}^k - \mathbf{p}_{t+\Delta t}^{k-1}\|_\infty \geq \varepsilon \vee k = 0$
  10.     Set  $\mathbf{p}_t^k = \vartheta \mathbf{p}_{t+\Delta t}^k + (1 - \vartheta)\mathbf{p}_t$
  11.     Compute  $\mathbf{H} = \vartheta \Delta t \mathbf{K}(\mathbf{p}_t^k) + \mathbf{M}(\mathbf{p}_t^k)$
  12.     Compute  $\mathbf{P} = \mathbf{M}(\mathbf{p}_t^k) - (1 - \vartheta)\Delta t \mathbf{K}(\mathbf{p}_t^k)$
  13.     Compute  $\mathbf{f} = \Delta t[\vartheta \mathbf{b}_{t+\Delta t}(\mathbf{p}_t^k) + (1 - \vartheta)\mathbf{b}_t(\mathbf{p}_t^k)]$
  14.     Solve  $\mathbf{H}\mathbf{p}_{t+\Delta t}^{k+1} = \mathbf{P}\mathbf{p}_t + \mathbf{f}$
  15.     Update  $\sigma_z$  for all nodes in  $\Omega^f$
  16.     Update  $\kappa(\sigma_z)$ ,  $\phi(\sigma_z)$ ,  $\alpha(\sigma_z)$ ,  $\zeta(\sigma_z)$
  17.     Compute  $u(\mathbf{x}, t)$  for all nodes in  $\Omega^f$  and update the grid
  18.     Update  $k \leftarrow k + 1$
  19.   **End while**
  20.   Update  $t \leftarrow t + \Delta t$  and  $\mathbf{p}_t$
  21.   Add new polygons on top of the grid
  22. **End while**
- 

#### 4. Numerical results

Numerical experiments are carried out to validate the VEM implementation and test its potentials in challenging applications. First, the numerical accuracy of the VEM solution is compared to that of the linear Finite Element Method (FEM) for different grid shapes and sizes. Then, the potential advantages of the flexible VEM discretization in alleviating the problems related to the grid distortion are investigated. Finally, the proposed approach is used in a real-world application, simulating the formation and progradation of the Vietnamese Mekong delta [42]. In particular, a mesh coarsening strategy is introduced in order to join automatically adjacent deformed elements, thus reducing the overall grid size and keep under control the computational complexity increase in long-term real-world applications. In all numerical simulations, we set  $\vartheta = 1$ .

##### 4.1. Validation and accuracy

For validation and numerical accuracy purposes, the proposed VEM model is first tested in the prediction of the long-term vertical dynamics of coastal environments, such as salt-marshes. We use as benchmark results those obtained in the same application by the linear FEM developed and validated by Zoccarato and Teatini [14].

We assume the marsh accretion in time to be due to the deposition of organic sediments with hydromechanical relationships obtained from data available in the literature. Here, oedometric tests performed on highly organic samples collected from low marsh and mudflat at the Cowpen Marsh (Tees Estuary, UK) are used to characterize the geomechanical properties  $\alpha$ ,  $\zeta$  and  $\phi$  of the marshland deposits [12,14]. The principal components of the hydraulic conductivity tensor  $\kappa_x$  and  $\kappa_z$  along the horizontal and vertical direction, respectively, are preliminarily assumed to be independent of  $\sigma_z$  and constant within each cross-section  $\Omega^f$ . Typical conductivity values for this type of soil are  $\kappa_z = 10^{-7}$  m/s and  $\kappa_x = 10\kappa_z$  [12]. A uniform in space and constant in time sedimentation rate  $\omega = 2$  mm/yr is applied as a loading condition on the salt-marsh top boundary  $\Gamma_{D,t}^f$ . As a result of the homogeneity of the sediments and the uniformity of the deposition rate, for any  $t \in [0, T]$  the domain  $\Omega^f$  has a rectangular shape with basis length  $L = 10.0$  m. A constant time-step size  $\Delta t = 0.5$  year is prescribed, for a total simulation time  $T = 500$  years.

To evaluate the numerical accuracy of the VEM model, a reference solution,  $p^*(\mathbf{x}, t)$ , is considered for  $t_1 = 100$  years,  $t_2 = 200$  years, and  $t_3 = 300$  years. Such a solution is obtained by regularly refining the triangulations used in the domains

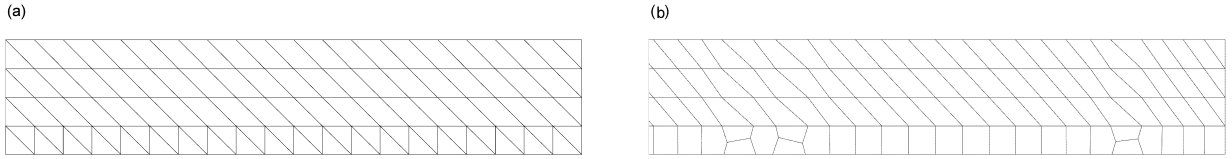


**Fig. 2.** Accuracy test case: zoom on the VEM computational grid generated by a random combination of triangles and quadrangles (a) and by the Polymesher utility (b).

**Table 1**

Accuracy test case: relative error  $\varepsilon_h(t)$  with respect to the reference solution for the FEM and VEM approaches at different  $h$  and  $t$ .

	$h$ [m]	$t_1$	$t_2$	$t_3$
Linear FEM	0.1	$6.48 \cdot 10^{-3}$	$6.06 \cdot 10^{-3}$	$5.97 \cdot 10^{-3}$
	0.05	$2.72 \cdot 10^{-3}$	$2.67 \cdot 10^{-3}$	$2.64 \cdot 10^{-3}$
	0.025	$9.25 \cdot 10^{-4}$	$9.19 \cdot 10^{-4}$	$9.07 \cdot 10^{-4}$
Lowest-order VEM <sup>(1)</sup>	0.1	$6.24 \cdot 10^{-3}$	$4.93 \cdot 10^{-3}$	$5.01 \cdot 10^{-3}$
	0.05	$2.47 \cdot 10^{-3}$	$2.35 \cdot 10^{-3}$	$2.39 \cdot 10^{-3}$
	0.025	$8.41 \cdot 10^{-4}$	$8.40 \cdot 10^{-4}$	$8.49 \cdot 10^{-4}$
Lowest-order VEM <sup>(2)</sup>	0.1	$1.24 \cdot 10^{-2}$	$5.16 \cdot 10^{-3}$	$4.88 \cdot 10^{-3}$
	0.05	$3.20 \cdot 10^{-3}$	$2.37 \cdot 10^{-3}$	$2.38 \cdot 10^{-3}$
	0.025	$8.91 \cdot 10^{-4}$	$8.32 \cdot 10^{-4}$	$8.43 \cdot 10^{-4}$

<sup>(1)</sup> Random combination of triangles and quadrangles (Fig. 2a).

<sup>(2)</sup> Polygonal grid built by the Polymesher utility (Fig. 2b).

$\Omega^{t_1}$ ,  $\Omega^{t_2}$ , and  $\Omega^{t_3}$  for solving the model (1)–(7) by linear FEM. The reference solution  $p^*(\mathbf{x}, t)$  is defined as the one obtained on the finest grid, such that the theoretical error convergence of linear FEM with  $h^2$  is noticed for the  $h$  values reported in Table 1, being  $h$  as usual the characteristic size of each triangulation. In particular, the value of  $h$  is assumed as the regular distance between two consecutive nodes along the  $x$  direction. The relative error of the numerical solution  $p_h(\mathbf{x}, t)$  with respect to the reference solution  $p^*(\mathbf{x}, t)$ :

$$\varepsilon_h(t) = \frac{\|p_h(\mathbf{x}, t) - p^*(\mathbf{x}, t)\|_0}{\|p^*(\mathbf{x}, t)\|_0} \quad (44)$$

is computed for both the FEM and VEM approach with different values of  $h$ . The results at  $t_1$ ,  $t_2$  and  $t_3$  for the grid resolution  $h = 0.1, 0.05, 0.025$ , are provided in Table 1. While the FEM grids are structured triangles with a constant spacing  $h$  between the nodes along the  $x$  direction, the computational grids used for the VEM approach are: (i) a combination of triangles and quadrangles with a constant spacing  $h$  between the nodes (Fig. 2a); (ii) a general polygonal partition built with the Polymesher utility [43] and a combination of triangles and quadrangles with an average horizontal spacing between the nodes equal to  $h$  (Fig. 2b). Inspection of Table 1 shows that the proposed VEM approach exhibits a numerical accuracy that is comparable to standard linear FEM, or even slightly better in most cases, though allowing a greater flexibility in the mesh construction.

Using the general set-up of the previous test problem, we assume now heterogeneous properties for the marsh sediments. The heterogeneity of the material properties generally leads to a high variability of the deformation pattern within the model domain, as already verified in [14], even though a uniform in space and constant in time sedimentation rate is assumed. The VEM simulation of the landform accretion is obtained by randomly assigning to the newly added elements on the top of the domain the properties of two materials, which describe typical organic and inorganic deposits. A virgin compression model,  $e = e_0 - C_c \log_{10}(\sigma_z)$ , is used to characterize the behavior of the void ratio,  $e$ , with the vertical effective stress,  $\sigma_z$ , for both materials, where  $C_c$  is the compression index and  $e_0$  the void ratio at the depositional surface. Values of  $C_c$  and  $e_0$  equal to 0.3 and 1.3 are used for Material 1, while Material 2 is softer with  $C_c = 0.6$  and  $e_0 = 2.3$ . The random distribution of sediment properties during the marsh accretion is shown as an example for three time values,  $t_1 = 100$ ,  $t_2 = 300$  and  $t_3 = 500$  years, in Fig. 3. The problem domain  $\Omega^t$  grows in size as the simulation proceeds, with the introduction of new triangular and quadrangular elements. The computational grid of the initial domain  $\Omega^0$  consists of a combination of general polygons built by the Polymesher utility [43].

The VEM solution, i.e., pressure and vertical displacements, is shown in Fig. 4. A typical drawback observed with the standard FEM in this heterogeneous setting is that local severe distortion in the element shape may occur, possibly affecting the solution accuracy [14]. The flexibility in the mesh generation guaranteed by the VEM approach, however, can reduce this difficulty. For instance, the grid can be expanded as the simulation proceeds by adding polygons that follow the patch of the heterogeneity and are joined to existing adjacent elements with the same material properties. Table 2 compares the maximum and average distortion of the grid elements as the simulation proceeds obtained with linear FEM and the

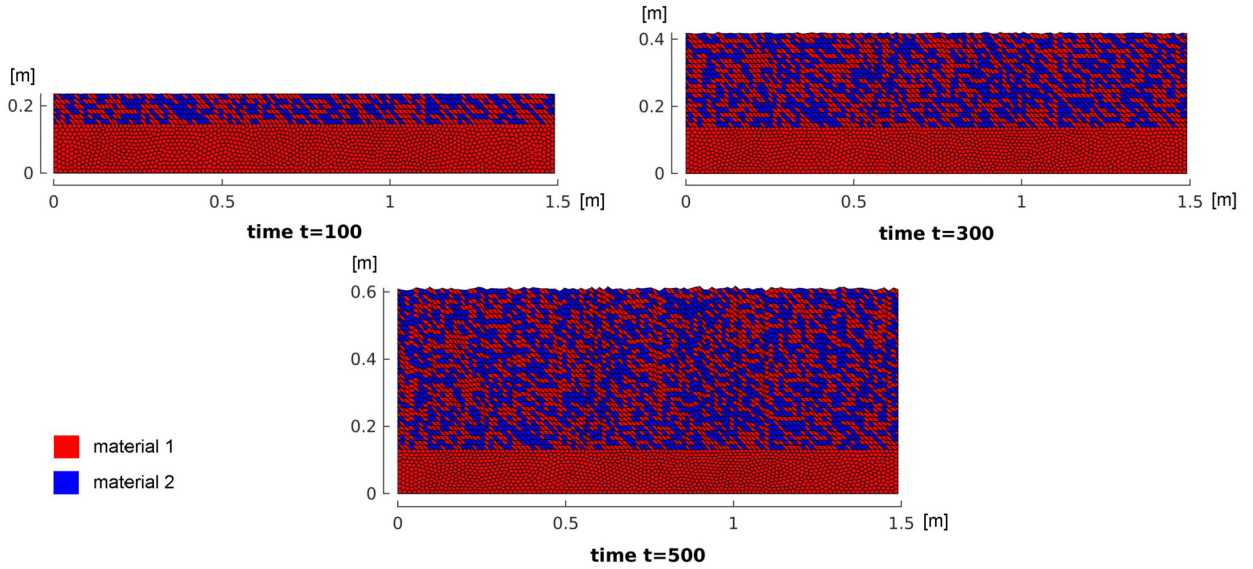


Fig. 3. Heterogeneous test case: computational grids and material distribution at  $t_1 = 100$ ,  $t_2 = 300$  and  $t_3 = 500$  years.

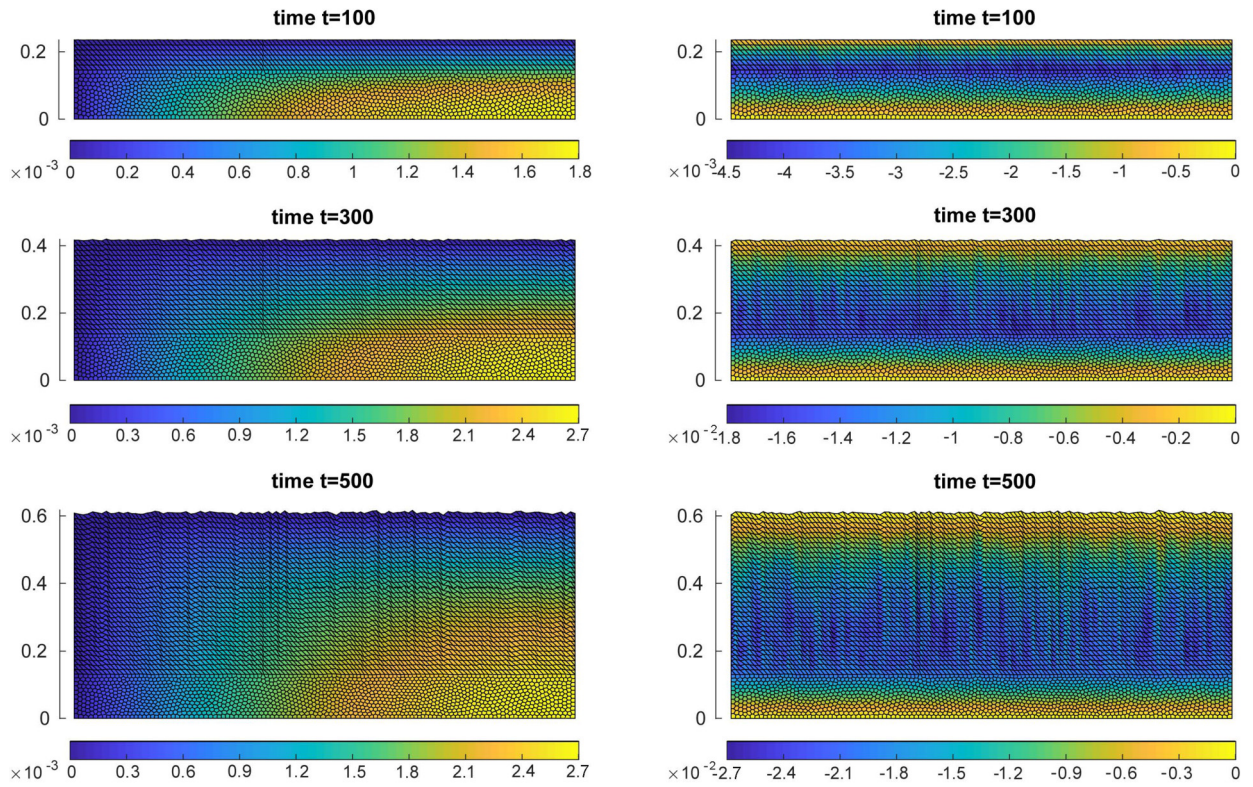


Fig. 4. Heterogeneous test case: pressure  $p_h(\mathbf{x}, t)$  [m] (left) and vertical displacement  $u(\mathbf{x}, t)$  [m] (right) at  $t_1 = 100$ ,  $t_2 = 300$  and  $t_3 = 500$  years. (For interpretation of the colors in the figure(s), the reader is referred to the web version of this article.)

proposed VEM models. The distortion  $\delta_k^t$  of the element  $\Omega_k^t$  at time  $t$  is measured as the ratio between its largest and smallest side,  $\ell_{k,\max}^t$  and  $\ell_{k,\min}^t$ , respectively:

$$\delta_k^t = \frac{\ell_{k,\max}^t}{\ell_{k,\min}^t}, \quad \forall \Omega_k^t \in \Omega^t. \tag{45}$$

**Table 2**

Heterogeneous test case: maximum and average ratio between the elemental distortion  $\delta_k^t$  and the initial value  $\delta_k^0$  for the FEM and VEM approaches at different simulation times  $t$ .

	Linear FEM				VEM			
	$t_0 = 0$	$t_1 = 100$	$t_2 = 300$	$t_3 = 500$	$t_0 = 0$	$t_1 = 100$	$t_2 = 300$	$t_3 = 500$
$\max_k(\delta_k^t/\delta_k^0)$	1.000	1.145	1.613	2.285	1.000	1.038	1.052	1.059
$\text{avg}_k(\delta_k^t/\delta_k^0)$	1.000	1.011	1.031	1.076	1.000	1.017	1.036	1.050

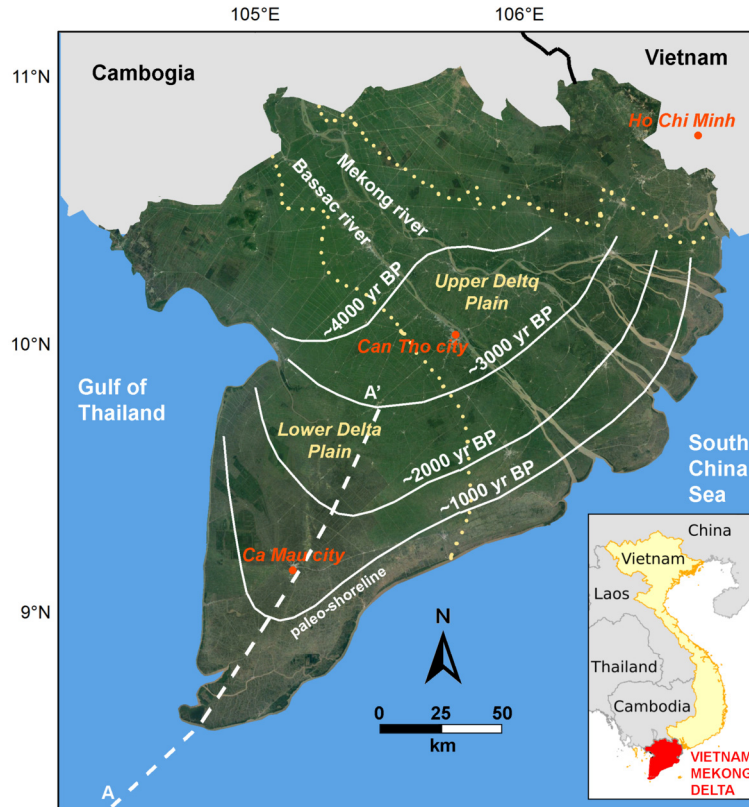


Fig. 5. The Mekong river delta area.

Table 2 provides the maximum and average ratio between  $\delta_k^t$  and the initial value  $\delta_k^0$  for  $t_1 = 100$ ,  $t_2 = 300$ , and  $t_3 = 500$  years. Though the average distortion evolves mildly and in a similar way for both approaches, with linear FEM strong local element deformations are possible. In the worst case, a triangular element can be distorted more than twice as much its initial condition. By distinction, the polygons characterizing the VEM grid generally preserve their shape, because they can better follow the physical distribution of the heterogeneous material parameters.

#### 4.2. Real-world application: the Mekong river delta test case

A challenging real-world application is finally discussed using the proposed VEM approach. The formation and evolution of the Vietnamese Mekong delta (Fig. 5) over the past 4,000 years has been recently investigated in [44] using the modeling approach proposed in [14], thus representing a significant benchmark for our methodology. The main objective of the numerical study was to simulate the deposition of mainly unconsolidated sediments during the second half of the Holocene, followed by high compaction rates, up to about 20 mm/yr, due to natural consolidation. This process has a very significant impact from both a social and environmental viewpoint, as it can seriously threaten the delta plain with permanent inundation and increase the vulnerability of the coastal area exposed to global sea level rise, flooding, salinization and human activities [45–48].

Over the past 4,000 yrs, the delta moved about 200 km in seaward direction (Fig. 5). Accumulation of fine-grained material from the Mekong river mouths resulted in a shoreline migration at an average progradation rate of 50 m/yr [49] and generated the Ca Mau peninsula. These sediments, mainly consisting of clay and organic clay, accumulated to a total thickness varying between 18 and 25 m on top of the older Pleistocene deposits. Our VEM model assesses the spatio-temporal

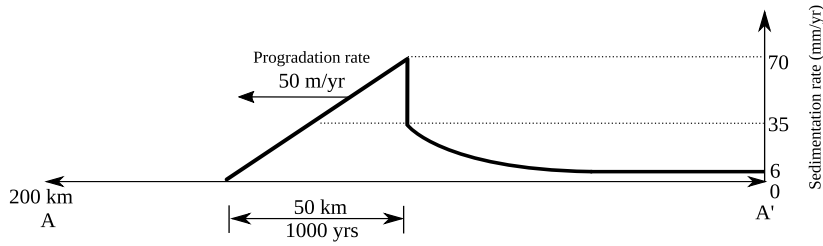


Fig. 6. Sedimentation rate in space and time used in the Mekong river delta case along the A-A' section (Fig. 5).

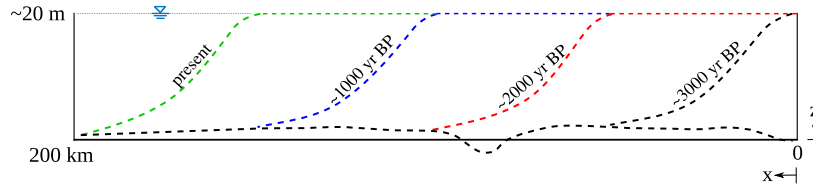


Fig. 7. Mekong river delta test case: evolution of the sedimentary formation according to the available data.

compaction and deformation of such sediments following the delta progradation, according to the set-up defined in [44]. The initial domain  $\Omega^0$  is a rectangle 0.2 m-high and 200 km-large discretized by 1,000 nodes and 998 triangular elements. Then, new elements are added on top of  $\Omega^0$  with a progressive deformation according to the evolving consolidation process and the load of the overlying sediment increase. The sedimentation rate  $\omega(x, t)$  varies according to the behavior provided in Fig. 6, as obtained by the interpretation of lithological investigations and sedimentation measurements. The delta formation was simulated with  $\omega(x, t)$  varying linearly from 0 to 70 mm/yr with shoreline proximity over a distance of 50 km in 1,000 yrs. After 1,000 yrs, i.e., at 3,000 yrs before present (BP), the delta was completely formed. At this stage, a dynamic balance of sediment accumulation and compaction allows the delta plain to sustain its elevation. The values of  $\omega(x, t)$  progressively decrease moving inland from the shoreline because of the compaction rate reduction due to the reduced overpressure, hence less sediment is needed to fill the accommodation. On the upper delta plain, a constant sedimentation rate of 6 mm/yr suffices to counterbalance sediment compaction. According to the available information, Fig. 7 shows the expected model evolution at 3,000, 2,000, 1,000 yrs BP and present.

Experimental data on lithological boreholes and geotechnical profiles in Ca Mau revealed the presence of two main sediment types, i.e., very soft organic clays overlying soft mineral clays [50]. The organic material is characterized by  $e_0 = 2.5$  and  $C_c = 1.05$ , while values of  $e_0 = 1.89$  and  $C_c = 0.57$  are used for the mineral clays. More details on the material properties are provided in [44]. The simulation spans 4,000 yrs with a time step  $\Delta t = 1$  year.

The modeling approach followed in [44] has a computational grid that increases at every time step, growing up to the final size of 103,799 nodes and 206,372 triangles. Moreover, it may suffer from the numerical issues linked to a high distortion of the triangular elements, resulting from the large deformations occurring over a long simulation time period. Such drawbacks are addressed by the VEM approach by defining a mesh coarsening strategy that merges adjacent elements characterized by a distortion larger than some user-specified threshold. This procedure allows to keep under control both the increase of the model size and the element distortion, and exploits the VEM flexibility in the domain partitioning.

The coarsening procedure operates as follows. At the simulation beginning, the maximum elemental area,  $A_{\max}$ , is computed. Then, at every time step, we mark the elements lying in the interior of the domain whose area,  $A^E$ , is such that

$$A^E < A_{\max} \cdot \varepsilon, \quad (46)$$

being  $\varepsilon$  a user-specified tolerance (set to 0.8 in our simulation). We mark only interior elements for the sake of simplicity. Each element is conventionally defined by the list of its vertices, i.e., the nodes, set in a counter-clockwise order. Therefore, the elemental edges  $e$  can be naturally defined in the same order by considering pairs of consecutive node indices. For each marked element  $E^*$  satisfying condition (46), the following procedure is applied:

1. define the set  $\mathcal{N}^{E^*}$  of neighboring elements, i.e., those with at least a node in common with the ones of  $E^*$ . The elements in  $\mathcal{N}^{E^*}$  that had been already used in the coarsening procedure and those exceeding a user-specified maximum number of nodes  $N_{\max}^E$  define the subset  $\mathcal{N}_{\text{excl}}^{E^*} \subseteq \mathcal{N}^{E^*}$  of the elements that will be excluded from the coarsening process. The remaining elements, lying in  $\mathcal{N}_{\text{incl}}^{E^*} \equiv \mathcal{N}^{E^*} \setminus \mathcal{N}_{\text{excl}}^{E^*}$ , will collapse with  $E^*$  into a new element;
2. if the neighbor  $E \in \mathcal{N}_{\text{incl}}^{E^*}$ , we remove the common edges with  $E^*$  and keep the remaining ones with their orientation. Because of the way the edges are numbered, the edge  $(i, j)$  of  $E$  is in common with  $E^*$  if and only if  $(j, i)$  belongs to  $E^*$ ;
3. if the neighbor  $E \in \mathcal{N}_{\text{excl}}^{E^*}$ , we just keep the common edges with  $E^*$  according to the  $E^*$  orientation;

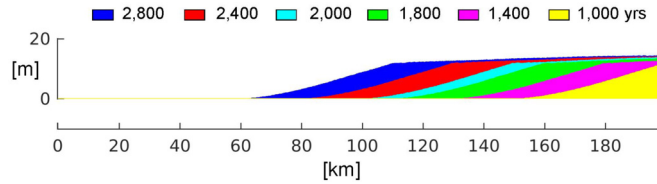


Fig. 8. Mekong river delta test case: simulated evolution of the sedimentary formation at 2,800 yrs according to the VEM model.

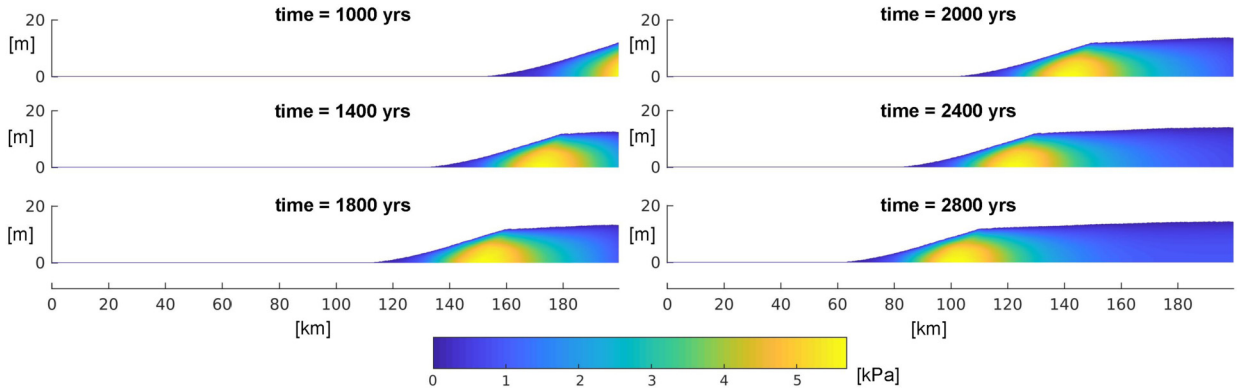


Fig. 9. Mekong river delta test case: pore pressure solution at different time values.

Table 3

Mekong river delta test case: evolution of the number of nodes and elements during the long-term simulation. The rightmost column shows the ratio between the number of nodes with VEM and FEM.

Time [yrs]	VEM		FEM		Ratio
	# elements	# nodes	# elements	# nodes	
0	998	1,000	998	1,000	1.00
1,000	6,141	4,076	15,430	7,793	0.52
1,100	7,440	4,535	19,958	10,080	0.45
1,200	8,801	4,950	24,726	12,488	0.40
1,300	10,211	5,385	29,738	15,019	0.36
1,400	11,722	5,827	34,927	17,640	0.33
1,500	13,231	6,268	40,304	20,355	0.31
1,800	17,998	7,547	57,309	28,944	0.26
2,000	21,293	8,369	69,298	34,999	0.24
2,400	28,174	10,028	84,785	42,821	0.23
2,800	35,228	11,616	120,478	60,847	0.19

- the edges inherited by  $E^*$  are ordered such that the second vertex is the first one of the next edge, eliminating the duplicates;
- if a node is the first (or the second) vertex in more than one edge, then the coarse element has holes and  $E^*$  cannot be correctly joined with the neighbors. In this case, the original grid is restored.

Internal nodes, i.e., element vertices not included in the list of the edges, are removed. Finally, after the coarsening procedure is completed, we reorder the elements and the nodes of the mesh. A numerical example showing in detail how the coarsening strategy works is described in Appendix B.

The evolution of the computational domain to simulate the Mekong delta progradation is shown in Fig. 8, while the pore pressure solution is provided at a few representative times in Fig. 9. The modeling outcome is in good agreement with the one presented in [44] and is consistent with the geological information available in the area (Fig. 7). Over the past 4,000 years, the lower delta plain elevation remained approximately constant with respect to the sea level, as a result of the dynamic balance of sediment accumulation and compaction. The sediment compaction, due to delayed overpressure dissipation, created room for new deposits, which sustained the elevation and the total thickness of the sedimentary layer. The maximum value of the overpressure is obtained at the bottom of the sedimentary column at the shoreline, where sedimentation rate has its largest value. Then, overpressure is smaller seaward, because of the smaller sediment thickness, and inward, where it has already partially dissipated.

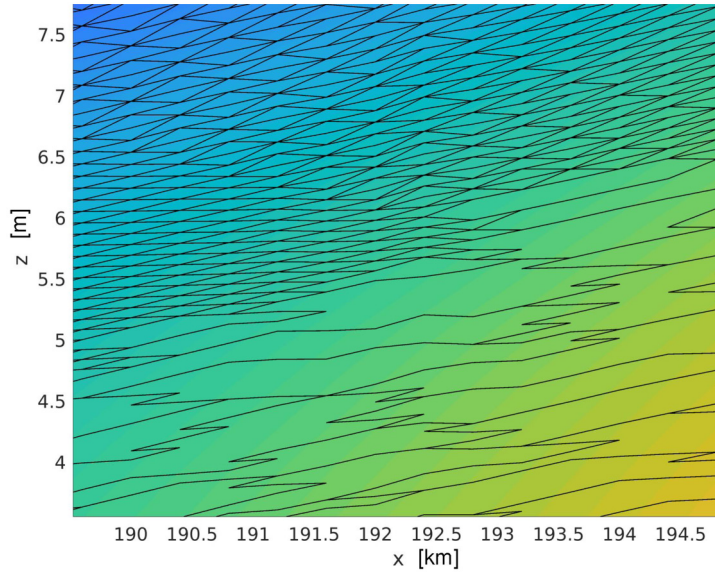


Fig. 10. Mekong river delta test case: example of coarsened grid.

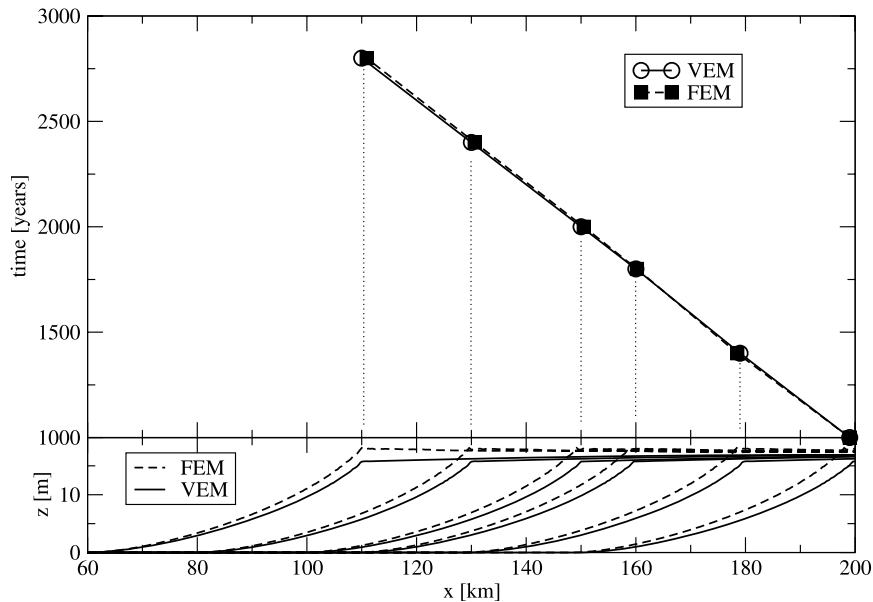


Fig. 11. Mekong river delta test case: comparison between the VEM and FEM solution. Shoreline progression (above) and sedimentary column evolution (below) vs time.

Notice that the computational grid is strongly anisotropic and the elements can be deformed very severely during the simulation of the delta progradation. However, with the coarsening strategy described above the number of elements and nodes of the overall grid, though increasing because of the domain evolution, remains under control. An example of the effect of the coarsening strategy on the computational grid is shown in Fig. 10. Table 3 shows a comparison between the model size required for solving the same problem by VEM and FEM. The computational gain provided by the VEM increases as the simulation proceeds, with the overall problem size reduced to less than 20% of the FEM size. Such a reduction does not impact in a significant way on the solution accuracy, as it can be appreciated in Fig. 11 that shows the shoreline progression in time predicted by the two models. The outcome is practically indistinguishable, with a slight difference in the evolution of the total size of the sedimentary column. Such a difference is due to the update of  $\kappa$ ,  $\alpha$ ,  $\phi$ , and  $\zeta$  (line 16 of Algorithm 1), which is carried out by approximating these quantities with piecewise constant functions at the elemental level.

## 5. Conclusions

A novel numerical model for the long-term dynamics prediction of transitional environments, such as lagoons, salt-marshes or river deltas, is developed in this work with the aid of the Virtual Element Method. The VEM use appears to be particularly promising in this kind of simulations, because the combined effect of sediment accretion and consolidation, i.e., the two main processes driving the dynamics of such environments, typically gives rise to a significant geometric non-linearity, which may result in a pronounced grid distortion using standard grid-based discretization methods. By distinction, using the VEM approach allows for the stable use of very irregular meshes consisting of a free combination of different polygonal elements, thus ensuring a great flexibility in the element generation and management.

The long-term dynamics of transitional landforms is simulated by coupling a 2D non-linear groundwater flow equation with a 1D geomechanical module in a Lagrangian framework with large deformations. The numerical model is based on the framework developed in [14] with the introduction of the VEM discretization. New elements are added to adjust the evolution of the computational domain and a practical coarsening algorithm is advanced to automatically join adjacent cells undergoing an excessive distortion, thus allowing to keep under control the overall model size. Accuracy and robustness of the proposed approach is tested both in academic examples of salt-marsh accretion and in the long-term evolution of the Mekong river delta, Vietnam.

The following results are worth summarizing.

- The VEM approach is a recent grid-based variational technique, which to our knowledge has been used here in one of the first real-world model applications. Real-world problems typically involve a number of issues, such as geometric and material non-linearities, which can provide useful pieces of information on the actual method applicability. In this sense, VEM has proved a robust, accurate and viable alternative to standard FEM in the simulation of the long-term coupled dynamics of transitional environments.
- The flexibility in the choice of different polygonal elements to discretize evolving computational domains can reduce the element distortion possibly arising by using standard FEM. Especially in long-term simulations spanning thousands of years, this helps alleviate such an occurrence, which is typically induced in this application by the presence of heterogeneous media.
- A coarsening strategy has been introduced to automatically merge elements suffering from an excessive distortion. This solution is allowed by the flexibility of VEM in the domain partitioning and can help reduce the overall size of real-world models without any significant loss of accuracy.

## Declaration of competing interest

The authors declare that they have no known competing financial interests or personal relationships that could have appeared to influence the work reported in this paper.

## Acknowledgements

This work is part of the VENEZIA-2021 Research Programme, Topic 3.1, funded by the “Provveditorato Interregionale Opere Pubbliche per il Veneto, Trentino Alto Adige e Friuli Venezia Giulia” through the “Concessionario Consorzio Venezia Nuova” and coordinated by CORILA, Venice.

## Appendix A. Virtual element vectors and matrices

The construction of the local consistency and stability matrices is based on the matrix representation of the projection operator  $\Pi_1^\nabla$ . The full description can be found for instance in [26]. In the sequel we provide few details only on some practical aspects.

The local stiffness consistency matrix is equal to

$$\mathbf{K}_C^{VEM} = (\mathbf{\Pi}_*^\nabla)^T \tilde{\mathbf{G}} \mathbf{\Pi}_*^\nabla \quad (\text{A.1})$$

where  $\tilde{\mathbf{G}}$  entries read:

$$\left(\tilde{\mathbf{G}}\right)_{ij} = \int_E \frac{\kappa}{\gamma} \nabla m_i \cdot \nabla m_j \, d\mathbf{x}, \quad i, j = 1, 2, 3 \quad (\text{A.2})$$

and  $\mathbf{\Pi}_*^\nabla$  is defined as:

$$\mathbf{\Pi}_*^\nabla = \mathbf{G}^{-1} \mathbf{B} \quad (\text{A.3})$$

with  $\mathbf{G}$  and  $\mathbf{B}$  matrices of size  $3 \times 3$  and  $3 \times N^E$ . The matrix  $\tilde{\mathbf{G}}$  of equation (A.2) is obtained with the assumption that  $\kappa$  is diagonal in the reference frame  $(x, z)$  and is approximated by a constant at the elemental level. As far as  $\mathbf{G}$  is concerned, two

possible ways are available to build it and it is useful to use both of them in order to check the implementation correctness. Here we provide only the simplest strategy:

$$\mathbf{G} = \mathbf{B}\mathbf{D} \tag{A.4}$$

with

$$\mathbf{D} = \begin{pmatrix} m_1(\mathbf{x}_1^E) & m_2(\mathbf{x}_1^E) & m_3(\mathbf{x}_1^E) \\ m_1(\mathbf{x}_2^E) & m_2(\mathbf{x}_2^E) & m_3(\mathbf{x}_2^E) \\ \vdots & \vdots & \vdots \\ m_1(\mathbf{x}_{NE}^E) & m_2(\mathbf{x}_{NE}^E) & m_3(\mathbf{x}_{NE}^E) \end{pmatrix} \tag{A.5}$$

and

$$\mathbf{B} = \begin{pmatrix} \overline{\varphi_1} & \dots & \overline{\varphi_{NE}} \\ \int_E \nabla m_2 \cdot \nabla \varphi_1 \, d\mathbf{x} & \dots & \int_E \nabla m_2 \cdot \nabla \varphi_{NE} \, d\mathbf{x} \\ \int_E \nabla m_3 \cdot \nabla \varphi_1 \, d\mathbf{x} & \dots & \int_E \nabla m_3 \cdot \nabla \varphi_{NE} \, d\mathbf{x} \end{pmatrix} \tag{A.6}$$

where  $m_i, i = 1, 2, 3$ , are the basis functions of  $\mathcal{P}_1(E)$  (equation (18)) and  $\varphi_i, i = 1, \dots, NE$ , are the basis functions of  $\mathcal{V}_{h|E}$  (equations (23) and (27)). The explicit computation of  $\mathbf{B}$  is performed by recalling that  $\overline{\varphi_i} = 1/NE$  and that:

$$\begin{aligned} \int_E \nabla \varphi_i \, d\mathbf{x} &= \oint_{\partial E} \varphi_i \cdot \mathbf{m} \, ds \\ &= \frac{1}{2} (|e_{i-1}| \mathbf{m}_{i-1} + |e_i| \mathbf{m}_i) \end{aligned} \tag{A.7}$$

where  $|e_i|$  is the length of element edge  $e_i$  and  $\mathbf{m}_i$  is the outer normal to  $e_i$ . If  $\mathbf{d}_i$  denotes the vector joining the vertices  $\mathbf{x}_{i-1}$  and  $\mathbf{x}_{i+1}$ ,  $\mathbf{d}_i^\perp = [d_{i,1}^\perp, d_{i,2}^\perp]^T$  is a clockwise rotation by  $90^\circ$  of  $\mathbf{d}_i$ . Then, from (A.7), we have:

$$\int_E \nabla \varphi_i \, d\mathbf{x} = \frac{1}{2} \mathbf{d}_i^\perp \tag{A.8}$$

and

$$\mathbf{B} = \frac{1}{2h_E NE} \begin{pmatrix} 2h_E & 2h_E & \dots & 2h_E \\ d_{1,1}^\perp NE & d_{2,1}^\perp NE & \dots & d_{NE,1}^\perp NE \\ d_{1,2}^\perp NE & d_{2,2}^\perp NE & \dots & d_{NE,2}^\perp NE \end{pmatrix} \tag{A.9}$$

The local stiffness stability matrix  $\mathbf{K}_S^{VEM}$  is arbitrary. A simple way to compute it is:

$$\mathbf{K}_S^{VEM} = \xi (\mathbf{I} - \mathbf{\Pi}^\nabla)^T (\mathbf{I} - \mathbf{\Pi}^\nabla) \tag{A.10}$$

where  $\mathbf{I}$  is the identity of order  $NE$ ,  $\mathbf{\Pi}^\nabla = \mathbf{D}\mathbf{\Pi}_*^\nabla$ , and  $\xi$  is a user-specified positive constant. For instance, in [51,52]  $\xi$  is a lumped approximation of the diffusion tensor  $\boldsymbol{\kappa}/\gamma$  components:

$$\xi = \text{Trace}(\boldsymbol{\kappa}) \frac{|E|}{\gamma h_E^2} \tag{A.11}$$

Similar expressions are obtained for the mass matrix. The local mass consistency matrix can be written as:

$$\mathbf{M}_C^{VEM} = (\mathbf{\Pi}_*^0)^T \tilde{\mathbf{H}} \mathbf{\Pi}_*^0 \tag{A.12}$$

where  $\tilde{\mathbf{H}}$  is matrix with entries:

$$(\tilde{\mathbf{H}})_{ij} = \int_E \psi m_i m_j \, d\mathbf{x}, \quad i, j = 1, 2, 3 \tag{A.13}$$

and  $\mathbf{\Pi}_*^0$  reads:

$$\mathbf{\Pi}_*^0 = \mathbf{H}^{-1} \mathbf{C} \tag{A.14}$$

with  $\mathbf{H}$  a  $3 \times 3$  matrix whose entries are given by

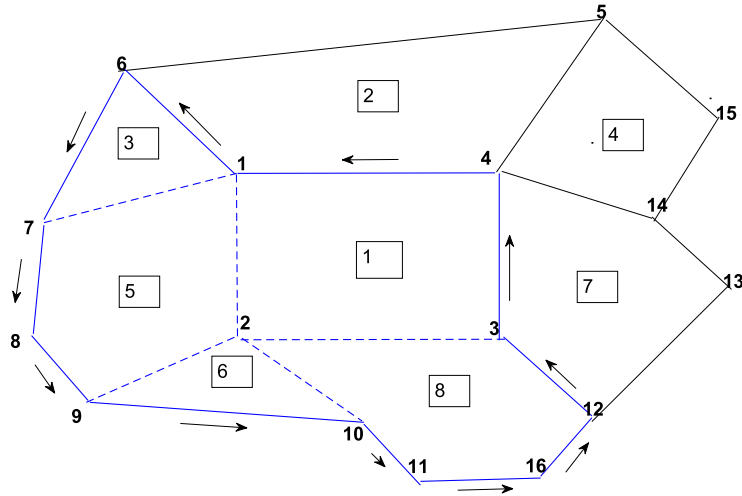


Fig. B.12. Example of mesh and the related coarsening procedure.

$$(\mathbf{H})_{ij} = \int_E m_i m_j \, d\mathbf{x}, \quad i, j = 1, 2, 3. \tag{A.15}$$

With VEM, we have  $\mathbf{C} = \mathbf{H}\mathbf{G}^{-1}\mathbf{B}$ ,  $\mathbf{G}$  and  $\mathbf{B}$  being the matrices (A.4) and (A.9) already constructed for the stiffness part. Hence,  $\mathbf{\Pi}_*^0 = \mathbf{\Pi}_*^\nabla$  as expected. The stability mass matrix can be approximated as:

$$\mathbf{M}_S^{VEM} = \bar{\psi} \frac{|E|}{h_E^2} (\mathbf{I} - \mathbf{\Pi}^0)^T (\mathbf{I} - \mathbf{\Pi}^0) \tag{A.16}$$

where  $\bar{\psi}$  is a lumped coefficient taking into account of  $\psi$  at the elemental level and  $\mathbf{\Pi}^0 = \mathbf{\Pi}^\nabla$ .

**Appendix B. Coarsening strategy**

Consider the elements of Fig. B.12 and assume that element  $E^* = 1$  is marked for coarsening. The set of neighboring elements  $\mathcal{N}^1$  is defined by the elements labeled from number 2 to number 8. Let us suppose that  $\mathcal{N}_{excl}^1 = \{2, 4, 7\}$  and  $\mathcal{N}_{incl}^1 = \{3, 5, 6, 8\}$ . The edges of  $E^* = 1$  are the rows of the matrix:

$$\mathcal{E}^1 = \begin{pmatrix} 1 & 2 \\ 2 & 3 \\ 3 & 4 \\ 4 & 1 \end{pmatrix} \tag{B.1}$$

The union of the edges of the elements in  $\mathcal{N}_{incl}^1$ , excluding those in common with  $E^*$ , gives:

$$\mathcal{E}_{coarse}^1 = \begin{pmatrix} 7 & 1 \\ 1 & 6 \\ 6 & 7 \\ 9 & 2 \\ 1 & 7 \\ 7 & 8 \\ 8 & 9 \\ 2 & 9 \\ 9 & 10 \\ 10 & 2 \\ 11 & 16 \\ 16 & 12 \\ 12 & 3 \\ 2 & 10 \\ 10 & 11 \end{pmatrix} \tag{B.2}$$

Then, we add the edges of the elements in  $\mathcal{N}_{exl}^1$  in common with  $E^*$ , i.e., (3 4) and (4 1), and delete the common edges, that is those rows  $i$  and  $j$  of  $\mathcal{E}_{coarse}^1$  such that  $\mathcal{E}_{coarse}^1(i, 1) = \mathcal{E}_{coarse}^1(j, 2)$  and  $\mathcal{E}_{coarse}^1(i, 2) = \mathcal{E}_{coarse}^1(j, 1)$ :

$$\mathcal{E}_{coarse}^1 = \begin{pmatrix} 1 & 6 \\ 6 & 7 \\ 7 & 8 \\ 8 & 9 \\ 9 & 10 \\ 11 & 16 \\ 16 & 12 \\ 12 & 3 \\ 10 & 11 \\ 3 & 4 \\ 4 & 1 \end{pmatrix} \quad (\text{B.3})$$

Finally, we reorder the matrix in such a way  $\mathcal{E}_{coarse}^1(j, i) = \mathcal{E}_{coarse}^1(j-1, 2)$ :

$$\mathcal{E}_{coarse}^1 = \begin{pmatrix} 1 & 6 \\ 6 & 7 \\ 7 & 8 \\ 8 & 9 \\ 9 & 10 \\ 10 & 11 \\ 11 & 16 \\ 16 & 12 \\ 12 & 3 \\ 3 & 4 \\ 4 & 1 \end{pmatrix} \quad (\text{B.4})$$

The first column of  $\mathcal{E}_{coarse}^1$  is the list of nodes of the coarsened element in counter-clockwise order. The node 2 and the elements labeled 1, 3, 5, 6, 8 will be removed since they merged into the new one.

## References

- [1] J.T. Morris, P.V. Sundareshwar, C.T. Nietch, B. Kjerfve, D.R. Cahoon, Response of coastal wetlands to rising sea level, *Ecology* 83 (10) (2002) 2869–2877, [https://doi.org/10.1890/0012-9658\(2002\)083\[2869:ROCWTR\]2.0.CO;2](https://doi.org/10.1890/0012-9658(2002)083[2869:ROCWTR]2.0.CO;2).
- [2] R.J. Edwards, Mid- to late-Holocene relative sea-level change in southwest Britain and the influence of sediment compaction, *Holocene* 16 (4) (2006) 575–587, <https://doi.org/10.1191/0959683606hl941rp>.
- [3] M.J. Brain, A.J. Long, S.A. Woodroffe, D.N. Petley, D.G. Milledge, A.C. Parnell, Modelling the effects of sediment compaction on salt marsh reconstructions of recent sea-level rise, *Earth Planet. Sci. Lett.* 345–348 (2012) 180–193, <https://doi.org/10.1016/j.epsl.2012.06.045>.
- [4] M.J. Brain, A.C. Kemp, B.P. Horton, S.J. Culver, A.C. Parnell, N. Cahill, Quantifying the contribution of sediment compaction to late Holocene salt-marsh sea-level reconstructions, *Quat. Res.* 83 (1) (2015) 41–51, <https://doi.org/10.1016/j.yqres.2014.08.003>.
- [5] M. Roner, A. D'Alpaos, M. Ghinassi, M. Marani, S. Silvestri, E. Franceschinis, N. Realdon, Spatial variation of salt-marsh organic and inorganic deposition and organic carbon accumulation: inferences from the Venice lagoon, Italy, *Adv. Water Resour.* 93 (2015) 276–287, <https://doi.org/10.1016/j.advwatres.2015.11.011>.
- [6] M.J. Brain, A.C. Kemp, A.D. Hawkes, S.E. Engelhart, C.H. Vane, N. Cahill, T.D. Hill, J.P. Donnelly, B.P. Horton, Exploring mechanisms of compaction in salt-marsh sediments using Common Era relative sea-level reconstructions, *Quat. Sci. Rev.* 167 (2017) 96–111, <https://doi.org/10.1016/j.quascirev.2017.04.027>.
- [7] J.P. Liu, D.J. DeMaster, T.T. Nguyen, Y. Saito, V.L. Nguyen, X. Li, Stratigraphic formation of the Mekong river delta and its recent shoreline changes, *Oceanography* 30 (2017) 72–83, <https://doi.org/10.5670/oceanog.2017.316>.
- [8] J.R.L. Allen, Morphodynamics of Holocene salt marshes: a review sketch from the Atlantic and Southern North Sea coasts of Europe, *Quat. Sci. Rev.* 19 (2000) 1155–1231, [https://doi.org/10.1016/S0277-3791\(99\)00034-7](https://doi.org/10.1016/S0277-3791(99)00034-7).
- [9] J.R.L. Allen, Geological impact on coastal wetland landscapes: some general effects of sediment autocompaction in the Holocene of northwest Europe, *Holocene* 9 (1) (1999) 1–12, <https://doi.org/10.1191/095968399674929672>.
- [10] N.D. Sheldon, G.J. Retallack, Equation for compaction of paleosols due to burial, *Geology* 29 (3) (2001) 247–250, [https://doi.org/10.1130/0091-7613\(2001\)029<0247:EFCDPD>2.0.CO;2](https://doi.org/10.1130/0091-7613(2001)029<0247:EFCDPD>2.0.CO;2).
- [11] M. Marani, A. D'Alpaos, S. Lanzoni, L. Carniello, A. Rinaldo, Biologically-controlled multiple equilibria of tidal landforms and the fate of the Venice lagoon, *Geophys. Res. Lett.* 34 (11) (2007) 1–5, <https://doi.org/10.1029/2007GL030178>.
- [12] M.J. Brain, A.J. Long, D.N. Petley, B.P. Horton, R.J. Allison, Compression behaviour of minerogenic low energy intertidal sediments, *Sediment. Geol.* 233 (1–4) (2011) 28–41, <https://doi.org/10.1016/j.sedgeo.2010.10.005>.
- [13] A. D'Alpaos, C. Da Lio, M. Marani, Biogeomorphology of tidal landforms: physical and biological processes shaping the tidal landscape, *Ecology* 5 (5) (2012) 550–562, <https://doi.org/10.1002/eco.279>.
- [14] C. Zoccarato, P. Teatini, Numerical simulations of Holocene salt-marsh dynamics under the hypothesis of large soil deformations, *Adv. Water Resour.* 110 (2017) 107–119, <https://doi.org/10.1016/j.advwatres.2017.10.006>.
- [15] T. Belytschko, D. Organ, Y. Krongauz, A coupled finite element-element-free Galerkin method, *Comput. Mech.* 17 (1995) 186–195.
- [16] S. Fernandez-Mendez, A. Huerta, Enrichment and coupling of the finite element and meshless methods, *Int. J. Numer. Methods Eng.* 48 (2000) 1615–1636.

- [17] T. Chen, I. Rajui, A coupled finite element and meshless local Petrov-Galerkin method for two-dimensional potential problems, *Comput. Methods Appl. Mech. Eng.* 192 (2003) 4533–4550.
- [18] V. Nguyen, T. Rabczuk, S. Bordas, M. Duflot, Meshless methods: a review and computer implementation aspects, *Math. Comput. Simul.* 79 (2008) 763–813.
- [19] Z. Ullah, W. Coombs, C. Augarde, An adaptive finite element/meshless coupled method based on local maximum entropy shape functions for linear and nonlinear problems, *Comput. Methods Appl. Mech. Eng.* 267 (2013) 111–132.
- [20] A. Zanette, M. Ferronato, C. Janna, Enriching the finite element method with meshfree particles in structural mechanics, *Int. J. Numer. Methods Eng.* 110 (2017) 675–700, <https://doi.org/10.1002/nme.5437>.
- [21] B. Giovanardi, A. Scotti, L. Formaggia, A hybrid XFEM–Phase field (*Xfield*) method for crack propagation in brittle elastic materials, *Comput. Methods Appl. Mech. Eng.* 320 (2017) 396–420, <https://doi.org/10.1016/j.cma.2017.03.039>.
- [22] M. Ferronato, A. Mazzia, G. Pini, G. Gambolati, A meshless method for axis-symmetric poroelastic simulations: numerical study, *Int. J. Numer. Methods Eng.* 70 (2007) 1346–1375.
- [23] A. Deeks, C. Augarde, A hybrid meshless local Petrov-Galerkin method for unbounded domains, *Comput. Methods Appl. Mech. Eng.* 196 (2007) 843–852.
- [24] L. Beirão da Veiga, K. Lipnikov, G. Manzini, *The Mimetic Finite Difference Method for Elliptic Problems*, Springer, 2014.
- [25] L. Beirão da Veiga, F. Brezzi, A. Cangiani, G. Manzini, L. Marini, A. Russo, Basic principles of virtual element methods, *Math. Models Methods Appl. Sci.* 23 (1) (2013) 199–214, <https://doi.org/10.1142/S0218202512500492>.
- [26] L. Beirão da Veiga, F. Brezzi, L. Marini, A. Russo, The hitchhiker's guide to the virtual element method, *Math. Models Methods Appl. Sci.* 24 (8) (2014) 1541–1573, <https://doi.org/10.1142/S021820251440003X>.
- [27] L. Beirão da Veiga, F. Brezzi, L. Marini, Virtual elements for linear elasticity problems, *SIAM J. Numer. Anal.* 51 (2) (2013) 794–812.
- [28] A. Gain, C. Talischi, G. Paulinho, On the virtual element method for three-dimensional linear elasticity problems on arbitrary polyhedral meshes, *Comput. Methods Appl. Mech. Eng.* 282 (2014) 132–160.
- [29] F. Benedetto, S. Berrone, S. Pieraccini, S. Scialò, The virtual element method for discrete fracture network simulations, *Comput. Methods Appl. Mech. Eng.* 280 (1) (2014) 135–156.
- [30] G. Vacca, L. Beirão da Veiga, Virtual element method for parabolic problems on polygonal meshes, *Numer. Methods Partial Differ. Equ.* 31 (2015) 2110–2134.
- [31] F. Benedetto, S. Berrone, S. Scialò, A globally conforming method for solving flow in discrete fracture networks using the virtual element method, *Finite Elem. Anal. Des.* 109 (2016) 23–36.
- [32] F. Benedetto, S. Berrone, S. Pieraccini, S. Scialò, A hybrid mortar virtual element method for discrete fracture network simulations, *J. Comput. Phys.* 306 (2016) 148–156.
- [33] O. Andersen, M. Nilsen, X. Raynaud, Virtual element method for geomechanical simulations of reservoir models, *Comput. Geosci.* 21 (2017) 877–893, <https://doi.org/10.1007/s10596-017-9636-1>.
- [34] G. Gambolati, Equation for one-dimensional vertical flow of groundwater. 1. The rigorous theory, *Water Resour. Res.* 9 (4) (1973) 1022–1028.
- [35] G. Gambolati, Equation for one-dimensional vertical flow of groundwater. 2. Validity range of the diffusion equation, *Water Resour. Res.* 9 (5) (1973) 1385–1395.
- [36] S. van Asselen, E. Stouthamer, T.W.J. van Asch, Effects of peat compaction on delta evolution: a review on processes, responses, measuring and modeling, *Earth-Sci. Rev.* 92 (1–2) (2009) 35–51, <https://doi.org/10.1016/j.earscirev.2008.11.001>.
- [37] G. Gambolati, G. Giunta, P. Teatini, Numerical modeling of natural land subsidence over sedimentary basins undergoing large compaction, in: G. Gambolati (Ed.), *CENAS - Coastline Evolution of the Upper Adriatic Sea Due to Sea Level Rise and Natural and Anthropogenic Land Subsidence*, in: *Water Science and Technology Library*, vol. 28, Kluwer Academic Publ., 1998, pp. 77–102.
- [38] P. Grisvard, *Elliptic Problems in Nonsmooth Domains*, *Classics in Applied Mathematics*, vol. 69, SIAM, 2011.
- [39] B. Ahmadi, A. Alsaedi, F. Brezzi, L.D. Marini, A. Russo, Equivalent projectors for virtual element methods, *Comput. Math. Appl.* 66 (2013) 376–391, <https://doi.org/10.1016/j.camwa.2013.05.015>.
- [40] A. Cangiani, G. Manzini, A. Russo, N. Sukumar, Hourglass stabilization and the virtual element method, *Int. J. Numer. Methods Eng.* 102 (2015) 404–436, <https://doi.org/10.1002/nm.24854>.
- [41] L. Beirão da Veiga, F. Brezzi, L.D. Marini, A. Russo, Virtual element implementation for general elliptic equations, in: G.R. Barrenechea, F. Brezzi, A. Cangiani, E.H. Georgoulis (Eds.), *Building Bridges: Connections and Challenges in Modern Approaches to Numerical Partial Differential Equations*, Springer, 2016, pp. 39–71.
- [42] F. Renaud, C. Kuenzer, *The Mekong Delta System. Interdisciplinary Analyses of a River Delta*, Springer, Netherlands, 2012.
- [43] C. Talischi, G.H. Paulino, A. Pereira, I.F.M. Menezes, PolyMesher: a general-purpose mesh generator for polygonal elements written in Matlab, *Struct. Multidiscip. Optim.* 45 (3) (2012) 309–328, <https://doi.org/10.1007/s00158-011-0706-z>.
- [44] C. Zoccarato, P.S. Minderhoud, P. Teatini, The role of sedimentation and natural compaction in a prograding delta: insights from the mega Mekong delta, Vietnam, *Sci. Rep.* 8 (1) (2018) 1–12, <https://doi.org/10.1038/s41598-018-29734-7>.
- [45] J. Ericson, C. Vorosmarty, S. Dingman, L. Ward, M. Meybeck, Effective sea-level rise and deltas: causes of change and human dimension implications, *Glob. Planet. Change* 50 (1–2) (2006) 63–82, <https://doi.org/10.1016/j.gioplacha.2005.07.004>.
- [46] C. Kuenzer, H. Guo, J. Huth, P. Leinenkugel, X. Li, S. Dech, Flood mapping and flood dynamics of the Mekong delta: ENVISAT-ASAR-WSM based time series analyses, *Remote Sens.* 5 (2) (2013) 687–715, <https://doi.org/10.3390/rs5020687>.
- [47] F.G. Renaud, T.T.H. Le, C. Lindener, V.T. Guong, Z. Sebesvari, Resilience and shifts in agro-ecosystems facing increasing sea-level rise and salinity intrusion in Ben Tre Province, Mekong delta, *Clim. Change* 133 (1) (2015) 69–84, <https://doi.org/10.1007/s10584-014-1113-4>.
- [48] P.S.J. Minderhoud, G. Erkens, V.H. Pham, V.T. Bui, L. Erban, H. Kooi, E. Stouthamer, Impacts of 25 years of groundwater extraction on subsidence in the Mekong delta, Vietnam, *Environ. Res. Lett.* 12 (6) (2017) 064006, <https://doi.org/10.1088/1748-9326/aa7146>.
- [49] T.K.O. Ta, V.L. Nguyen, M. Tateishi, I. Kobayashi, Y. Saito, T. Nakamura, Sediment facies and late holocene progradation of the Mekong river delta in Bentre province, southern Vietnam: an example of evolution from a tide-dominated to a tide- and wave-dominated delta, *Sediment. Geol.* 152 (3) (2002) 313–325, [https://doi.org/10.1016/S0037-0738\(02\)00098-2](https://doi.org/10.1016/S0037-0738(02)00098-2).
- [50] P. Giao, T. Thoang, L. Thuyen, N. Vu, Geotechnical characterization of the subsoil profile underlying the land subsidence monitoring points in Southern Vietnam delta, in: *Proceedings of 9th International Symposium on Lowland Technology*, 2014, pp. 429–436.
- [51] A. Cangiani, G. Manzini, O.J. Sutton, Conforming and nonconforming virtual element methods for elliptic problems, *IMA J. Numer. Anal.* 37 (2016) 1317–1354, <https://doi.org/10.1093/imanum/drw036>.
- [52] A. Cangiani, E.H. Georgoulis, T. Pryer, O.J. Sutton, A posteriori error estimates for the virtual element method, *Numer. Math.* 137 (4) (2017) 857–893, <https://doi.org/10.1007/s00211-017-0891-9>.